RSC Advances

PAPER

View Article Online
View Journal | View Issue

Cite this: *RSC Adv.*, 2019, **9**, 38724

The electrical properties and modulation of g-C_3N_4/β-As and g-C_3N_4/β-Sb heterostructures: a first principles study

Bo Liang,[ab] Yongchao Rao [a] and Xiangmei Duan *[ab]

Received 14th August 2019
Accepted 28th October 2019

DOI: 10.1039/c9ra06357a

rsc.li/rsc-advances

The electronic properties of the g-C_3N_4/β-As and g-C_3N_4/β-Sb heterojunctions are investigated *via* density functional theory. We find that both heterostructures are indirect band gap semiconductors that, when applied to a photocatalytic device, will suffer from inefficient light emission. Fortunately, the band gap of the two junctions can be adjusted by external biaxial strain. As strain increases from compression to extensive, both compounds undergo a transition from metals, indirect semiconductors to direct semiconductors. Moreover, due to the charge transfer, each junction forms a large built-in electric field, which helps to prevent the recombination of electrons and holes. Our results are expected to widen the potential applications of these heterojunctions in nanodevices.

1. Introduction

The successful exfoliation of single layer of graphite[1] led a revolution in two dimensional (2D) materials, which attracted widespread attention in the next few years for their special properties and potential applications. Graphene has excellent electron mobility,[2,3] high thermal stability[4] and conductivity,[5,6] great mechanical[7,8] and optical[9] properties. However, the lack of band gap seriously restricts its actual utilization in microelectronic devices. Researchers have been working on finding other 2D materials. Recently, hexagonal boron nitride (h-BN),[10,11] transition metal dichalcogenide (TMD),[12–14] graphitic carbon nitride,[15–18] and phosphorene[19–21] have been synthesized successfully. Thereafter, ultrathin 2D van der Waals heterojunctions and their devices have received extensive attention.[22,23]

Among the allotropes of the non-metallic carbon nitride, graphitic C_3N_4 (g-C_3N_4) is the most stable phase under ambient conditions.[24] It exhibits the characteristic of semiconductor (with a band gap of 2.7 eV[25]), and is non-toxic, visible light responsive and easy to synthesize.[26–28] In addition, g-C_3N_4 has caused great concern due to its conceivable usage in electronic devices and optoelectronic conversion.

For bulk arsenic and antimony, the most stable allotrope is beta gray arsenic and beta gray antimony, respectively. Both are buckled honeycomb structure analogous to blue phosphorus.[29] And their monolayer counterparts are known as gray arsenene (β-As) and gray antimonene (β-Sb), respectively. β-As and β-Sb sheets have been experimentally synthesized,[30–33] with a corresponding indirect band gap of 2.49 and 2.28 eV,[30] as well as considerable carrier mobility.[34–36] It is critical to have a tunable band gap for semiconductor materials, especially when applied to nanodevices. Previous studies have reported that the electronic structure of few-layer arsenic and antimony nanosheets depends sensitively on the number of layers, stacking modes and defects.[36–40] Meanwhile, β-As or β-Sb can be converted into direct band gap semiconductors under electric field and biaxial strain.[37,41,42] An interesting idea arises: can the electronic properties of β-As and β-Sb based heterostructures be modulated under strain?

In this paper, the electronic properties of g-C_3N_4/β-As and g-C_3N_4/β-Sb heterostructures are systematically investigated by using first-principles calculations. We find that the stable heterostructures can be readily formed due to the slight lattice mismatch between the compounds. The charge transfer between each junction results in a built-in electric field, which helps to prevent the recombination of electrons and holes. The heterostructures are indirect band gap semiconductors, however, their electronic properties could be tuned by the biaxial strain (ε).

2. Calculation methods

All the calculations are performed using the plane-wave basis Vienna *Ab initio* Simulation Package (VASP) code. The exchange–correlation potentials are described through the Perdew–Burke–Ernzerhof (PBE) functional within the generalized gradient approximation (GGA) formalism. A damped van der Waals correction (DFT-D2) based on Grimme's scheme is also incorporated to better describe the non-bonding interaction between the different layers.[43] The vacuum region is 20 Å to

[a]*School, of Physical Science and Technology, Ningbo University, 315211, China. E-mail: duanxiangmei@nbu.edu.cn*

[b]*Laboratory of Clean Energy Storage and Conversion, Ningbo University, Ningbo, 315211, China*

avoid the spurious interaction caused by the periodic boundary condition. A Morkhorst-pack k points mesh of $5 \times 5 \times 1$ and $11 \times 11 \times 1$ is used to sample the Brillouin zone for geometry optimization and calculating the density of states, respectively. The cutoff energy of the plane–wave is set to be 500 eV. All of the self-consistent loops are iterated until the total energy difference of the systems between the adjacent iterating steps less than 10^{-5} eV, and the structures are fully relaxed with a force tolerance of 0.005 eV Å^{-1}.

Binding energy, E_b, can be used to present the structural stability of the heterostructure system. For instance, the binding energy of g-C_3N_4 and β-As is defined as

$$E_b = (E_{\text{g-}C_3N_4/\beta\text{-As}} - E_{\text{g-}C_3N_4} - E_{\beta\text{-As}})/N$$

where $E_{\text{g-}C_3N_4/\beta\text{-As}}$, $E_{\text{g-}C_3N_4}$, and $E_{\beta\text{-As}}$ are the energy of the hybrid g-C_3N_4/β-As complex, g-C_3N_4 and β-As single layers, respectively. N is the total atomic number of the pristine g-C_3N_4 monolayer.

The charge density difference is determined by subtracting the electronic charge of the corresponding isolated compositions from the heterojunctions, for g-C_3N_4/β-Sb, that is, $\Delta\rho = \rho_{\text{g-}C_3N_4/\beta\text{-Sb}} - \rho_{\text{g-}C_3N_4} - \rho_{\beta\text{-Sb}}$, where $\rho_{\text{g-}C_3N_4/\beta\text{-Sb}}$, $\rho_{\text{g-}C_3N_4}$, and $\rho_{\beta\text{-Sb}}$ are the charge density of the corresponding g-C_3N_4/β-Sb heterostructure, g-C_3N_4 and β-Sb sheet. The amount of transferred charge $\Delta Q(z)$ is calculated by $\Delta Q(z) = \int_{-\infty}^{z} \Delta\rho(z')\mathrm{d}z'$.

The biaxial strain is defined as $\varepsilon = (l - l_0)/l_0 \times 100\%$, where l and l_0 is the strained and original lengths of the monolayer along one of strain direction. The sample is compressed or tensile in two distinct directions with the same strain level.

3. Results and discussion

As shown in Table 1, the optimized lattice parameters of g-C_3N_4, β-As, and β-Sb monolayers are 7.13, 3.62 and 4.06 Å, respectively, in good agreement with the previous theoretical and experimental reports (7.13, 3.68 and 4.01 Å).[25,30,34] For the three kinds of sheets, GGA-PBE shows the band gaps of 1.20, 1.63, and 1.12 eV, which agree well with the reported data (1.19, 1.64, and 1.18 eV).[34,44,45]

To simulate the g-C_3N_4/β-As and g-C_3N_4/β-Sb heterostructures, a 2×2 supercell for β-As and a $\sqrt{3} \times \sqrt{3}$ cell for β-Sb are used separately to match the 1×1 g-C_3N_4 unit cell. The lattice mismatch is only 1.54% (1.37%) respectively between β-As (β-Sb) and g-C_3N_4, which should be suitable for building hybrid structures. The top and side views of g-C_3N_4/β-As and g-C_3N_4/β-Sb heterostructures are illustrated in Fig. 1. The g-C_3N_4 and β-As sheets remain their pristine geometries with a vertical

Table 1 The lattice parameters (Å) and band gap (eV) for β-As, β-Sb and g-C_3N_4. The values in the brackets are taken from the references, the alphabet b, c, d, e, and f represent the ref. 21, 46, 35, 47 and 40, respectively

	g-C_3N_4	β-As	β-Sb
a (Å)	7.13 (7.13)[b]	3.62 (3.68)[c]	4.06 (4.01)[d]
E_g (eV)	1.20 (1.19)[e]	1.63 (1.64)[c]	1.12 (1.18)[f]

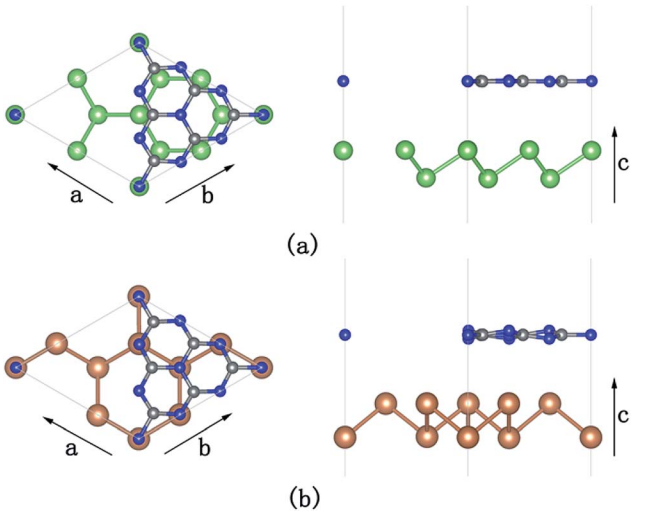

Fig. 1 Top (left panel) and side (right panel) views of g-C_3N_4/β-As (a) and g-C_3N_4/β-Sb (b). Blue, gray, green, and brown spheres represent the N, C, As, and Sb atoms, respectively.

distance of 3.44 Å. While in the junction of g-C_3N_4/β-Sb, the layer g-C_3N_4 tilts slightly, the average distance between the two counterparts is 3.42 Å. Therefore, the heterojunctions are connected by van der Waals interaction. The binding energy is calculated to be −37.14 meV and −42.86 meV for g-C_3N_4/β-As and g-C_3N_4/β-Sb, respectively, indicating the stability of both heterojunctions. The strength of the interaction is stronger than that of graphene/β-As (graphene/β-Sb) heterojunctions, in which E_b is −29.70 meV or −39.62 meV, as reported by similar DFT calculations.[46,47]

Band structure and density of states for the hybrid g-C_3N_4/β-As and g-C_3N_4/β-Sb are shown in Fig. 2. The PBE calculation gives an indirect band gap of 1.24 eV for g-C_3N_4/β-As and 0.83 eV for g-C_3N_4/β-Sb. For the former, the VBM locates at Γ point and CBM at K point. While for the latter, the VBM is located at Γ too and CBM at M. Intriguingly, a large dispersion of band nears the VBM of the g-C_3N_4/β-Sb can be observed, indicating the high mobility of photogenerated holes. While both the CBM and VBM of g-C_3N_4/β-As are relatively localized, meaning a low carrier mobility.

To quantitatively understand carrier migration, we calculate the effective mass of charge carriers by the formula $m^* = \hbar^2 \left(\frac{\partial^2 E}{\partial k^2}\right)^{-1}$ and list the results in Table 2. Generally, the values of effective masses along different directions have a large difference in g-C_3N_4/β-As and g-C_3N_4/β-Sb, confirming the obvious anisotropy in the heterojunctions. For β-As junction, the great values of holes, m_h^*, along the Γ–K and Γ–M directions, and the mass of electrons, m_e^*, along the K–M direction, reveal poor mobility of carrier migration. Fortunately, the mass m_e^* along the Γ–K direction is small, which provides the possibility for potential application of this material. In the case of g-C_3N_4/β-Sb, the effective masses of m_h^* along the Γ–K and Γ–M directions are reduced to 0.78 and 0.43 in comparison to the two

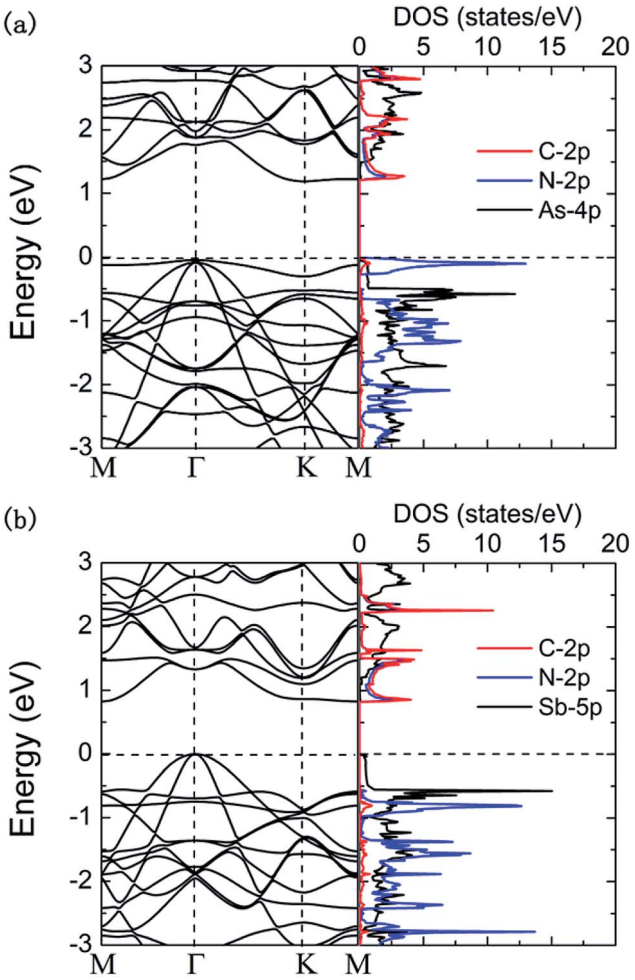

Fig. 2 The band structure and DOS of g-C_3N_4/β-As (a) and g-C_3N_4/β-Sb (b).

Table 2 Effective mass of two carriers (electron and hole) for β-As, β-Sb, g-C_3N_4, g-C_3N_4/β-As and g-C_3N_4/β-Sb, respectively

	m_e^* (Γ–K)	m_e^* (Γ–M)	m_e^* (K–M)	m_h^* (Γ–K)	m_h^* (Γ–M)
β-As	—	0.57	—	0.53	0.71
β-Sb	0.49	—	—	0.92	0.48
g-C_3N_4	0.83	—	2.86	4.87	2.66
g-C_3N_4/β-As	0.84	—	2.40	4.71	3.69
g-C_3N_4/β-Sb	—	0.62	4.29	0.78	0.43

separate sheets, which is expected to be used in photoelectronic devices.

From the partial density of states (PDOS) plots (shown in Fig. 2) of the two heterostructures, it can be seen that the VBM of g-C_3N_4/β-As is mainly contributed by the 2p states of N atoms and slightly by the 2p states of C atoms, its CBM consists of the 2p states of C atoms and N atoms, *i.e.* the VBM and CBM are mostly contributed by g-C_3N_4 side. In the case of g-C_3N_4/β-Sb, the VBM is attributed by 5p states of the Sb atoms, in contrast, the CBM is composed of the 2p states of C atoms and N atoms. More intuitively, the orbital diagrams in Fig. 3 shows that the

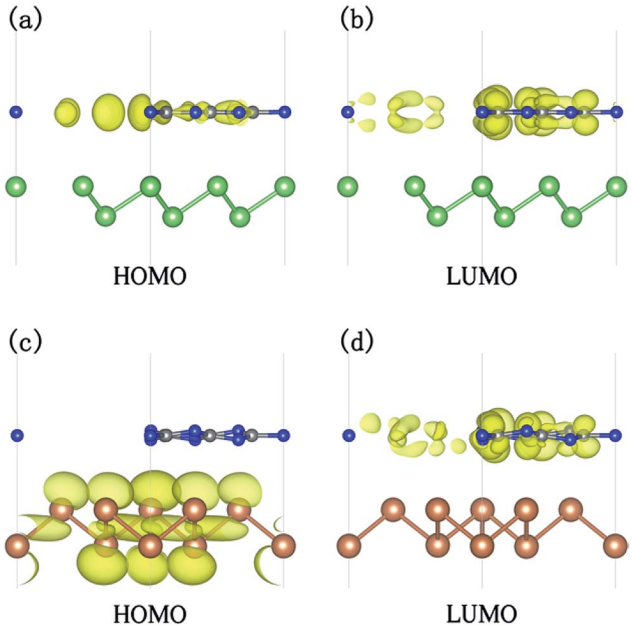

Fig. 3 The charge density corresponding to the HOMO and LUMO states for g-C_3N_4/β-As (a and b) and g-C_3N_4/β-Sb (c and d) with an isosurface value of 0.004 e Å^{-3}.

VBM and CBM of g-C_3N_4/β-As are both located in the monolayer g-C_3N_4 [see (a) and (b)].

The band edge alignment tells that g-C_3N_4/β-As is a type-I heterojunction, with the HOMO and LUMO locating in the same material of heterostructure. Whereas, the HOMO and LUMO of g-C_3N_4/β-Sb are located in different parts. The HOMO (VBM at Γ point) is mainly composed of the Sb atoms, while the LUMO (CBM at M point) is primarily contributed by the C atoms and N atoms from g-C_3N_4 side, indicating a type-II heterojunction, which has lower carrier recombination rate due to the separation of photogenerated electrons and holes, therefore it has higher carrier mobility and stronger photocatalytic activity.

We further investigate the charge density difference and the amount of transferred charge. Fig. 4(a) and (c) present the redistribution of charge density in two systems. Additionally, the vertical lateral charge transfer is shown in Fig. 4(b and d). We note that for g-C_3N_4/β-Sb junction, the charge density is redistributed by forming triangular shaped electron- and hole-rich regions, *i.e.*, an electron–hole puddle within the β-Sb layer. The formation mechanism of electron–hole enrichment zone is due to the inhomogeneous planar g-C_3N_4 substrate. The planar averaged charge density difference in Fig. 4(b and d) shows that the g-C_3N_4 layer donates electrons to β-As or β-Sb side. Thus, the charge transfer between β-As or β-Sb and g-C_3N_4 introduces a built-in electric field, which produces a driving force to separate the photogenerated carriers to different monolayers.

It is well known that strain can significantly adjust the electronic properties of 2D materials, especially in the application of band engineering and device design. Since the systems g-C_3N_4/β-As and g-C_3N_4/β-Sb are all indirect band gap semiconductors, when applied to a photocatalytic device, they will

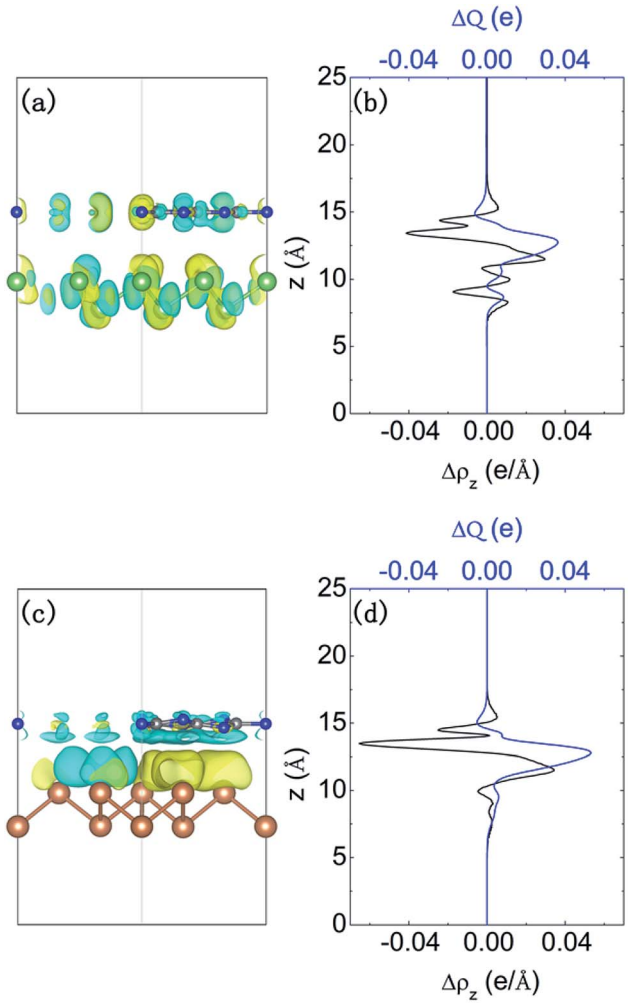

Fig. 4 Charge density difference (a) and (c), with an isosurface value of 0.0002 e Å^{-3}, the plane averaged differential charge density along the z direction $\Delta\rho$ and the amount of transferred charge ΔQ (b and d) for g-C_3N_4/β-As and g-C_3N_4/β-Sb junctions.

suffer from poorly efficient light emission. We next study how the geometric stability and electronic properties of heterojunctions change under external biaxial strain, for the intact strain range, we then focus on their band regulation. Fig. 5(a) presents the stress varies with the strain for the two junctions. It can be seen that g-C_3N_4/β-As keeps its structure intact under the strain from 12% compressive to 8% tensile, while g-C_3N_4/β-Sb can sustain a biaxial compressive and tensile strain up to 10% means that the structure of the membrane is robust under a strain.

Combining the Fig. 5(b) and (c), it can be seen that the band gap of g-C_3N_4/β-As and g-C_3N_4/β-Sb junctions have a significant regulation under external biaxial strain (ε). When ε is in the range of $[-6, 5]$, g-C_3N_4/β-As has an indirect band gap, which turns into a direct one when ε increases above 5%. A further decrease of ε less than −6%, the junction undergoes a transition from a semiconductor to a metal. Similarly, the g-C_3N_4/β-Sb exhibits metallic property when $\varepsilon \leq -6\%$. While it is still indirect band gap semiconductor in the strain range of $[-5, 9]$.

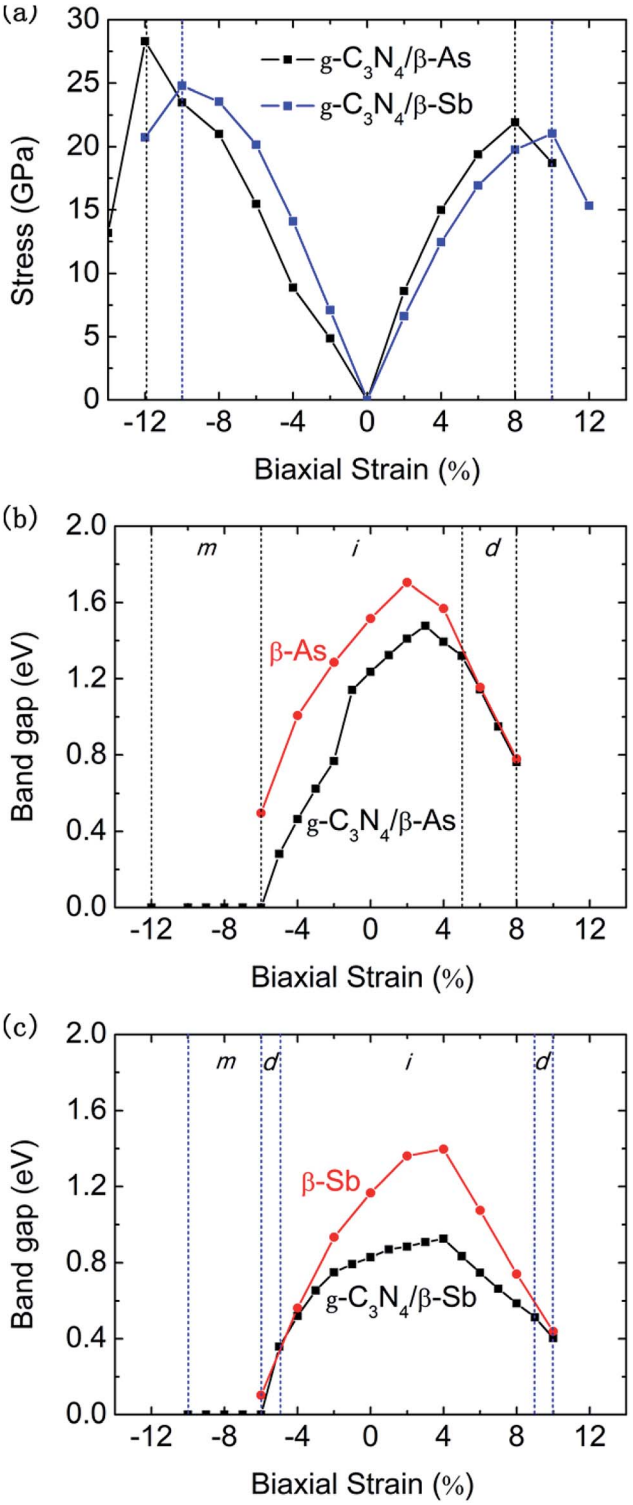

Fig. 5 (a) The stress of the junctions as a function of strain. Band gaps change under different biaxial strain of g-C_3N_4/β-As (b) and g-C_3N_4/β-Sb (c). Three regions are defined by the band type of the materials. m stands for metal, d and i represent the direct and indirect band gap of the semiconductors, respectively. The strain dependence of the band gap for isolated β-As and β-Sb are included for comparison.

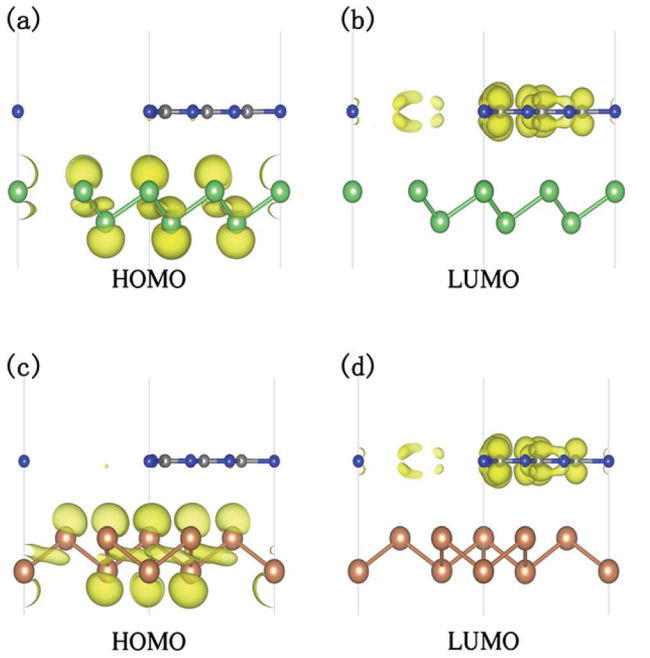

Fig. 6 The charge density distribution of the HOMO and LUMO states for g-C_3N_4/β-As at $\varepsilon = 6\%$ (a and b) and for g-C_3N_4/β-Sb under $\varepsilon = 10\%$ (c and d). The isosurface value is 0.004 e Å^{-3}.

When ε is in [−6, −5] and [9, 10], the junction experiences a transition from an indirect band gap semiconductor to a direct one. To figure out which part of the compounds dominate the change of the band structure under strain. We systematically investigate the electronic behavior of g-C_3N_4, β-As and β-Sb monolayers as a function of strain. As illustrated in Fig. 5(b) and (c), intriguingly, the variation trends of band gap for g-C_3N_4/β-As and g-C_3N_4/β-Sb are similar to the β-As and β-Sb, indicating β-As and β-Sb play a central role in the transition of the electronic characteristic of the junctions.

To reveal the mechanism for the transition of an indirect band gap semiconductor to a direct band gap, the electronic structure of g-C_3N_4/β-As at $\varepsilon = 6\%$ and g-C_3N_4/β-Sb at $\varepsilon = 10\%$ is compared with those of the unstrained system, respectively. For the junction containing β-As (β-Sb), the strain changes the CBM originally located at K (M) point to Γ point, while the location of VBM remains at Γ point. Moreover, the carrier distributions of the HOMO and LUMO states, as shown in Fig. 6, indicates the separation of electrons and holes for both systems, which is beneficial to prevent the recombination of the photogenerated carriers.

4. Conclusion

In summary, we have systematically investigated the electronic properties of the g-C_3N_4/β-As and g-C_3N_4/β-Sb junctions by density functional theory. The heterojunctions exhibit various electronic properties. Firstly, the g-C_3N_4/β-As is a type-I heterostructure, while the complex g-C_3N_4/β-Sb is a type-II junction. Secondly, the band gap of g-C_3N_4/β-Sb junction is significantly reduced, which promotes its adsorption of visible light. Thirdly, a certain amount of charge transfers between the layers of the two heterojunctions, and a large built-in electric field is formed to block the recombination of electrons and holes. Particularly, both compounds undergo a transition from the metals, the indirect semiconductors to direct semiconductors under strain. Our findings are beneficial to the development of high performance nanodevices in the future.

Conflicts of interest

There are no conflicts to declare.

Acknowledgements

This research is supported by the Natural Science Foundation of China (grant no. 11574167 and 11874033) and the KC Wong Magna Foundation in Ningbo University.

References

1 K. S. Novoselov, A. K. Geim, S. V. Morozov, D. Jiang, Y. Zhang, S. V. Dubonos, I. V. Grigorieva and A. A. Firsov, *Science*, 2004, **306**, 666–669.
2 K. S. Novoselov, A. K. Geim, S. V. Morozov, D. Jiang, M. I. Katsnelson, I. V. Grigorieva, S. V. Dubonos and A. A. Firsov, *Nature*, 2005, **438**, 197–200.
3 K. I. Bolotin, K. J. Sikes, Z. Jiang, M. Klima, G. Fudenberg, J. Hone, P. Kim and H. L. Stormer, *Solid State Commun.*, 2008, **146**, 351–355.
4 H. Y. Nan, Z. H. Ni, J. Wang, Z. Zafar, Z. X. Shi and Y. Y. Wang, *J. Raman Spectrosc.*, 2013, **44**, 1018–1021.
5 A. A. Balandin, S. Ghosh, W. Bao, I. Calizo, D. Teweldebrhan, F. Miao and C. N. Lau, *Nano Lett.*, 2008, **8**, 902–907.
6 H. Malekpour, K. H. Chang, J. C. Chen, C. Y. Lu, D. L. Nika, K. S. Novoselov and A. A. Balandin, *Nano Lett.*, 2014, **14**, 5155–5161.
7 C. Lee, X. Wei, J. W. Kysar and J. Hone, *Science*, 2008, **321**, 385–388.
8 R. Faccio, P. A. Denis, H. Pardo, C. Goyenola and Á. W. Mombrú, *J. Phys.: Condens. Matter*, 2009, **21**, 285304.
9 L. A. Falkovsky, *J. Phys.: Conf. Ser.*, 2008, **129**, 012004.
10 K. Watanabe, T. Taniguchi and H. Kanda, *Nat. Mater.*, 2004, **3**, 404–409.
11 L. Song, L. Ci, H. Lu, P. B. Sorokin, C. Jin, J. Ni, A. G. Kvashnin, D. G. Kvashnin, J. Lou, B. I. Yakobson and P. M. Ajayan, *Nano Lett.*, 2010, **10**, 3209–3215.
12 Q. H. Wang, K. Kalantar-Zadeh, A. Kis, J. N. Coleman and M. S. Strano, *Nat. Nanotechnol.*, 2012, **7**, 699.
13 M. Chhowalla, H. S. Shin, G. Eda, L.-J. Li, K. P. Loh and H. Zhang, *Nat. Chem.*, 2013, **5**, 263.
14 Y.-C. Rao, S. Yu and X.-M. Duan, *Phys. Chem. Chem. Phys.*, 2017, **19**, 17250–17255.
15 A. Thomas, A. Fischer, F. Goettmann, M. Antonietti, J.-O. Müller, R. Schlögl and J. M. Carlsson, *J. Mater. Chem.*, 2008, **18**, 4893–4908.
16 G. Gao, Y. Jiao, F. Ma, Y. Jiao, E. Waclawik and A. Du, *Phys. Chem. Chem. Phys.*, 2015, **17**, 31140–31144.

17 S. Yu, Y.-C. Rao, H.-H. Wu and X.-M. Duan, *Phys. Chem. Chem. Phys.*, 2018, **20**, 27970–27974.
18 Y.-C. Rao, Z.-Q. Chu, X. Gu and X.-M. Duan, *Comput. Mater. Sci.*, 2019, **161**, 53–57.
19 H. Liu, A. T. Neal, Z. Zhu, Z. Luo, X. Xu, D. Tománek and P. D. Ye, *ACS Nano*, 2014, **8**, 4033–4041.
20 L. Kou, C. Chen and S. C. Smith, *J. Phys. Chem. Lett.*, 2015, **6**, 2794–2805.
21 Y.-C. Rao, P. Zhang, S.-F. Li, X.-M. Duan and S.-H. Wei, *Phys. Chem. Chem. Phys.*, 2018, **20**, 12916–12922.
22 Y. Deng, Z. Luo, N. J. Conrad, H. Liu, Y. Gong, S. Najmaei, P. M. Ajayan, J. Lou, X. Xu and P. D. Ye, *ACS Nano*, 2014, **8**, 8292–8299.
23 W. Hu and J. Yang, *Comput. Mater. Sci.*, 2016, **112**, 518–526.
24 D. M. Teter and R. J. Hemley, *Science*, 1996, **271**, 53–55.
25 X. Wang, K. Maeda, A. Thomas, K. Takanabe, G. Xin, J. M. Carlsson, K. Domen and M. Antonietti, *Nat. Mater.*, 2008, **8**, 76.
26 J. Zhang, X. Chen, K. Takanabe, K. Maeda, K. Domen, J. D. Epping, X. Fu, M. Antonietti and X. Wang, *Angew. Chem., Int. Ed.*, 2010, **49**, 441–444.
27 J. Liu, T. Zhang, Z. Wang, G. Dawson and W. Chen, *J. Mater. Chem.*, 2011, **21**, 14398–14401.
28 S. Martha, A. Nashim and K. M. Parida, *J. Mater. Chem. A*, 2013, **1**, 7816–7824.
29 S. Zhang, M. Xie, F. Li, Z. Yan, Y. Li, E. Kan, W. Liu, Z. Chen and H. Zeng, *Angew. Chem., Int. Ed.*, 2016, **55**, 1666–1669.
30 G. Pizzi, M. Gibertini, E. Dib, N. Marzari, G. Iannaccone and G. Fiori, *Nat. Commun.*, 2016, **7**, 12585.
31 R. Gusmão, Z. Sofer, D. Bouša and M. Pumera, *Angew. Chem.*, 2017, **129**, 14609–14614.
32 Y. Wang, P. Huang, M. Ye, R. Quhe, Y. Pan, H. Zhang, H. Zhong, J. Shi and J. Lu, *Chem. Mater.*, 2017, **29**, 2191–2201.
33 X. Wu, Y. Shao, H. Liu, Z. Feng, Y.-L. Wang, J.-T. Sun, C. Liu, J.-O. Wang, Z.-L. Liu, S.-Y. Zhu, Y.-Q. Wang, S.-X. Du, Y.-G. Shi, K. Ibrahim and H.-J. Gao, *Adv. Mater.*, 2017, **29**, 1605407.
34 C. Kamal and M. Ezawa, *Phys. Rev. B: Condens. Matter Mater. Phys.*, 2015, **91**, 085423.
35 M. Fortin-Deschênes, O. Waller, T. O. Menteș, A. Locatelli, S. Mukherjee, F. Genuzio, P. L. Levesque, A. Hébert, R. Martel and O. Moutanabbir, *Nano Lett.*, 2017, **17**, 4970–4975.
36 K. Iordanidou, J. Kioseoglou, V. V. Afanas'ev, A. Stesmans and M. Houssa, *Phys. Chem. Chem. Phys.*, 2017, **19**, 9862–9871.
37 S. Zhang, Z. Yan, Y. Li, Z. Chen and H. Zeng, *Angew. Chem.*, 2015, **127**, 3155–3158.
38 Z. Zhang, J. Xie, D. Yang, Y. Wang, M. Si and D. Xue, *Appl. Phys. Express*, 2015, **8**, 055201.
39 L. Yang, Y. Song, W. Mi and X. Wang, *RSC Adv.*, 2016, **6**, 66140–66146.
40 X. Sun, Y. Liu, Z. Song, Y. Li, W. Wang, H. Lin, L. Wang and Y. Li, *J. Mater. Chem. C*, 2017, **5**, 4159–4166.
41 H. Shu, Y. Li, X. Niu and J. Guo, *J. Mater. Chem. C*, 2018, **6**, 83–90.
42 L. Kou, Y. Ma, X. Tan, T. Frauenheim, A. Du and S. Smith, *J. Phys. Chem. C*, 2015, **119**, 6918–6922.
43 S. Grimme, *J. Comput. Chem.*, 2006, **27**, 1787–1799.
44 F. Wu, Y. Liu, G. Yu, D. Shen, Y. Wang and E. Kan, *J. Phys. Chem. Lett.*, 2012, **3**, 3330–3334.
45 D. Singh, S. K. Gupta, Y. Sonvane and I. Lukačević, *J. Mater. Chem. C*, 2016, **4**, 6386–6390.
46 W. Li, T.-X. Wang, X.-Q. Dai, X.-L. Wang, Y.-Q. Ma, S.-S. Chang and Y.-N. Tang, *Phys. E*, 2017, **88**, 6–10.
47 H. V. Phuc, N. N. Hieu, B. D. Hoi, L. T. T. Phuong, N. V. Hieu and C. V. Nguyen, *Superlattices Microstruct.*, 2017, **112**, 554–560.